Matériaux & Techniques **110**, 203 (2022)

https://doi.org/10.1051/mattech/2022005

Matériaux & Techniques

Available online at:
www.mattech-journal.org

Special Issue on 'Indentation across scales and techniques: recent advances in experiments and modelling', edited by Vincent Keryvin

Regular Article

Open Access

A combined EBSD/nanoindentation study of dislocation density gradients near grain boundaries in a ferritic steel

Layal Chamma[1,2,*], Jean-Marc Pipard[1], Artem Arlazarov[1], Thiebaud Richeton[2], Jean-Sébastien Lecomte[2], and Stéphane Berbenni[2]

[1] ArcelorMittal Maizières Research SA, Voie Romaine, BP30320, 57283 Maizières-lès-Metz, France
[2] Université de Lorraine, Arts et Métiers Paris Tech, CNRS, LEM3, 57000 Metz, France

Received: 12 November 2021 / Accepted: 17 January 2022

Abstract. Microstructural internal lengths play an important role on the local and macroscopic mechanical behaviors of steels. In this study, the dislocation density gradients near grain boundaries in a ferritic steel are investigated using SEM/EBSD together with instrumented nanoindentation for undeformed and pre-deformed aluminum-killed steels (Al-k) at 3% and 18% tensile plastic strains. The effect of the distance to grain boundaries on Geometrically Necessary Dislocations (GND) densities is first determined by analyzing orientation gradients from 2D-EBSD maps. Then, nanohardness measurements are performed in the vicinity of grain boundaries. Data analyses show a clear correlation between the spatial gradients of GND density and the ones of nanohardness. Using a mechanistic model, the total dislocation densities are estimated from the measured nanohardness values. From both GND and total dislocation density profiles, the value of an internal length, denoted λ, is estimated from the analysis of dislocation density gradients near grain boundaries. At the end, the capabilities of 2D-EBSD and nanoindentation methods to assess this value are discussed.

Keywords: dislocation densities / grain boundaries / nanoindentation / EBSD / ferritic steel

1 Introduction

The development of new types of high strength and high ductility steels requires combined experimental and theoretical modeling to fully characterize their complex mechanical behavior. This depends on understanding the local behavior at the scale of the constituents as well as their mechanical interactions. Such interactions were mainly studied with micromechanical models that only consider the composite effect (i.e., the effect of phase volume fractions). However, the predictive capability of such models is limited because of the absence of internal length effect in their formulations. There are actually two types of internal lengths: (i) initial internal lengths (e.g., grain size) and (ii) deformation induced internal lengths like the layer thickness of "Geometrically Necessary Dislocations" (GND) densities accumulated around grain boundaries (GB) or phase boundaries caused by crystal lattice incompatibilities. While the first type is known from the initial microstructure observed with optical or electron microscopy (e.g., SEM), the second kind is more difficult to characterize from both theory and experiment.

A first approach, called the ILMF (Internal Length Mean Field) model, aimed to calibrate such induced internal length in a phenomenological way by fitting the macroscopic tensile stress-strain curves at different grain sizes [1]. In this formulation, the microstructure of ferritic steels was considered as a two-phase composite by introducing a layer with finite thickness, denoted λ, which represented the accumulation of GND near grain boundaries. The model was applied to ferritic steels with different grain sizes considering a same constant value of λ. Hence, λ was assumed independent of strain and grain size and was only fitted with macroscopic stress/strain curves. Therefore, in the present study, it is proposed to experimentally determine this induced internal length λ by combining both Electron-Back-Scattered Diffraction (EBSD) and nanoindentation methods at different plastic deformations and in different grain configurations.

On the one hand, the EBSD technique alone was already used to identify such microstructural internal lengths induced by plastic deformation [2,3]. For instance, Genée et al. [4] recently investigated the localization of plastic deformation in a deformed FeTiB2 composite under uniaxial tension using high-resolution 2D-EBSD. Internal lengths were analyzed calculating the average density of GNDs as a function of distances to the closest TiB2

* e-mail: layal.chamma@univ-lorraine.fr

Table 1. Chemical composition of Al-k steel (in wt.%).

C	Mn	Al	Ni	Cr	Mo	Cu	P	S	N
0.0353	0.1920	0.0400	0.0380	0.0230	0.0050	0.0210	0.0080	0.0070	0.0039

particles, ferrite grain boundaries, particle tips and ferrite triple points. The results showed that the average GND densities increased with plastic strain and reached higher values at low particle spacing and close to particle tips than near grain boundaries and triple points. Calcagnotto et al. [5] also used high-resolution EBSD (2D and 3D) to quantify the orientation gradients, pattern quality, and GND density variations at the ferrite-ferrite and ferrite-martensite interfaces for two ultrafine-grained dual-phase steels with different martensite island sizes and volume fractions. They found that even with very small martensite particles, strong local plastic deformation was induced in adjacent ferrite regions. The orientation gradients were higher near the ferrite-martensite boundaries than at the ferrite-ferrite interfaces. Mishra et al. [6] found that the local misorientation in aluminum samples deformed under tension was higher near the GBs and then decreased without any particular behavior towards the center of the grain where it became nearly constant.

On the other hand, the instrumented nanoindentation method was used to study the grain size effects and local mechanical response due to self-organization of dislocations in crystalline materials [7]. Thus, this method could be used to identify, in an original way, the internal lengths of the microstructure at the micron or submicron scale using local nanohardness measurements. The dependence of material nanohardness on the corresponding characteristic length exhibits a size effect. In crystalline metals, size effects are mainly governed by the nucleation and evolution of the dislocations network. The so-called "indentation size effect" reflects the increase in hardness due to decrease in penetration depth. Various models concerning the indentation size effect have been discussed in the literature. The model of Nix and Gao [8] is the most widely used to explain the experimental observation using a conical tip. This model is based on the concept of GNDs generated by the indenter which are contained in a hemispherical volume that evolves with the contact radius around the indentation. Voyiadjis and Zhang [9,10] studied the effects of grain boundary distance on the nanohardness responses in Al and Cu bicrystals. They found that the hardening effect increased as the indentation distance from the grain boundary decreased. This hardening effect was due to the interaction between the GNDs created by the indenter and the grain boundary. Moreover, it was observed that indentations closer to the grain boundary led to higher hardness values and that hardening was more pronounced at lower indentation depths. On the contrary, when the distance between indentations and grain boundaries was large enough, the response was similar to a single crystal material as in the Nix–Gao model [8]. Nanohardness near grain boundaries was also studied by Soifer et al. [11] in high purity Cu with grain sizes ranging from 5 to 50 μm. They found that the nanohardness increased by a factor of 1.5 as the grain boundary was approached, and the characteristic distance at which the grain boundary affected the nanohardness was in the range of 2 μm. Soer [12] characterized the nanoindentation response of Mo bicrystals as a function of the distance from grain boundary. His results showed that the nanohardness was higher in zones up to 1 μm from the grain boundaries than in the inner region of the grains. Weaver et al. [13] performed nanoindentation measurements on previously deformed Ta samples to evaluate and quantify heterogeneous deformation in grain boundary regions. The measurements were performed in the grain boundary regions with different misorientation angles for pyramidal and spherical tips. They found that the grains with high misorientation exhibited a nanohardness gradient between the GB and the grain interior.

It is noteworthy that most of these studies focused essentially on the effects of internal lengths associated to the initial microstructure of undeformed specimens. However, a combined analysis of the induced internal length λ as mentioned above, using both EBSD and nanoindentation on pre-deformed tensile specimen at different strains, has not been reported yet. In this paper, a single-phase polycrystalline ferritic steel (Al-k) with low carbon content produced by ArcelorMittal was studied, considering both undeformed and deformed tensile specimens. The induced internal length λ is identified from the gradients of GND and total dislocation densities obtained from 2D-EBSD and nanohardness measurements, respectively.

2 Materials and methods

2.1 Material and specimen preparation

An aluminum-killed steel (Al-k) has been provided by ArcelorMittal Research Center (Maizières-les-Metz, France). It is a cold-rolled and batch annealed single-phase polycrystalline ferritic steel used for deep drawing applications. The chemical composition of the investigated Al-k steel is given in Table 1. The average grain size is obtained from the EBSD measurements as a weighted average of equivalent grain diameters and is equal to 25.6 μm. This diameter is derived from the area of the equivalent circular grain. The Al-k steel was subjected to uniaxial tensile tests along the rolling direction (RD) at 3.5% and 20% engineering strains to investigate the evolution of GND density and nanohardness with increasing plastic deformation. Figures 1a and 1b show the true stress-true strain curves of both tensile specimens. The final plastic true strains are $\varepsilon_p = 3.4\%$ and $\varepsilon_p = 18.4\%$, respectively. In the whole manuscript, these samples will be referred to as $\varepsilon_p = 3\%$ and $\varepsilon_p = 18\%$.

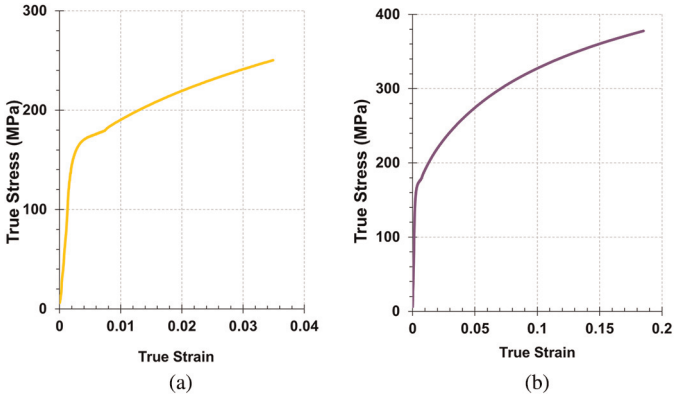

Fig. 1. True stress-strain curves of Al-k ferritic steel of both tensile specimens loaded up to respective plastic strains: (a) $\varepsilon_p = 3\%$ and (b) $\varepsilon_p = 18\%$.

Surface preparation is a very important first step for the SEM/EBSD analysis and for nanoindentation in order to obtain reliable elastic properties and nanohardness values. Initial mechanical polishing can introduce some deformation in the analyzed surface. Therefore, in this study, the initial preparation was done with the minimum force loads followed by polishing with 3 and 1 µm diamond disks. Then, additional polishing with a 0.04 µm colloidal silica suspension for 20 minutes was done to erase the introduced surface deformation.

2.2 Determination of GND densities from 2D-EBSD maps

EBSD maps were acquired using the CMOS-based "Symmetry" detector (full camera resolution: 1244×1024 pixels) and Oxford Instruments Aztec software on a Zeiss Auriga 40 FEG-SEM and a Jeol F100 at 15 kV with a tilt of 70°. The high-resolution maps were acquired and processed in refined accuracy mode. The global speed was approximately 48 Hz. Each map was acquired with a step size of 100 nm. The indexing rate was always above 98.5%.

EBSD analyses were performed in our study to evaluate the distribution of GND densities measured for each pixel and their evolution with plastic strain near the grain boundaries. All calculations and analyses of the EBSD maps were performed in the (RD, ND) plane using the MTEX algorithm [14]. GND densities are related to lattice incompatibilities and are obtained from the dislocation density tensor α_{ij} (also called Nye tensor). This tensor can be deduced from the lattice curvature tensor κ_{ij} defined as:

$$\kappa_{ij} = \frac{\partial \theta_i}{\partial x_j} \approx \frac{\Delta \theta_i}{\Delta x_j}, \tag{1}$$

with θ_i the local lattice orientation (rotation) vector and x_j the position vector. Equation (1) means that the components of the lattice curvature tensor κ_{ij} are estimated from the orientation gradients between a pixel and the neighboring pixels. Neglecting the curl of the elastic strain tensor, α_{ij} can be expressed as follows:

$$\alpha_{ij} = \kappa_{ji} - \delta_{ij}\kappa_{mm}. \tag{2}$$

This is the Nye's equation [15], where indices i, j range from 1 to 3 and the Einstein's notation is used. δ_{ij} and κ_{mm} denote the Kronecker delta and the trace of κ_{ij}, respectively. A scalar GND density can be estimated from the Nye tensor as: $\rho_{GND} = \frac{1}{b}\sqrt{\alpha_{ij}\alpha_{ij}}$. Since the local lattice orientations determined by classical EBSD are only in the 2D plane, only the six components κ_{i1} and κ_{i2} (with i = 1, 2, 3, denoting RD, ND and TD respectively) of the curvature tensor can be identified. In this case, five of the nine components of the dislocation density tensor can be calculated [16]. Therefore, the scalar GND density is approximated as:

$$\rho_{GND}^{EBSD} \approx \frac{1}{b}\sqrt{\alpha_{12}^2 + \alpha_{13}^2 + \alpha_{21}^2 + \alpha_{23}^2 + \alpha_{33}^2}, \tag{3}$$

where b is the Burgers vector's magnitude (0.251 nm for α-Fe). For the calculation of GND densities given by equations (1)–(3), a threshold value of 5° disorientation between two adjacent pixels was considered in our calculations. Therefore, adjacent pixels across grain boundaries that exhibit disorientation exceeding this value are not considered in the calculation.

2.3 Nanohardness measurements and total dislocation densities

Instrumented nanoindentation is used to obtain accurate local hardness measurements. In this experimental method, the nanohardness, denoted H, is defined as the average contact pressure, i.e., the ratio between the maximum applied load F_m and the projected contact area A_p between the indent and the sample surface at the maximum load:

$$H = \frac{F_m}{A_p}. \tag{4}$$

From the depth of indentation penetration and the known indent geometry, an indirect measure of contact area is obtained from which the nanohardness H can be estimated. The projected contact area function A_p varies with contact depth h_c. According to the analysis method reported by Oliver and Pharr [17,18], h_c can be calculated as follows:

$$h_c = h_m - \varepsilon\frac{F_m}{S}, \tag{5}$$

where h_m is the maximum depth, $S = dF/dh$ is the contact stiffness at F_m measured during unloading and ε is a geometric constant with tabulated values. The Oliver and Pharr's method assumes that the non-linear unloading curve follows a power law of the form:

$$F = \alpha_{OP}(h - h_p)^m, \tag{6}$$

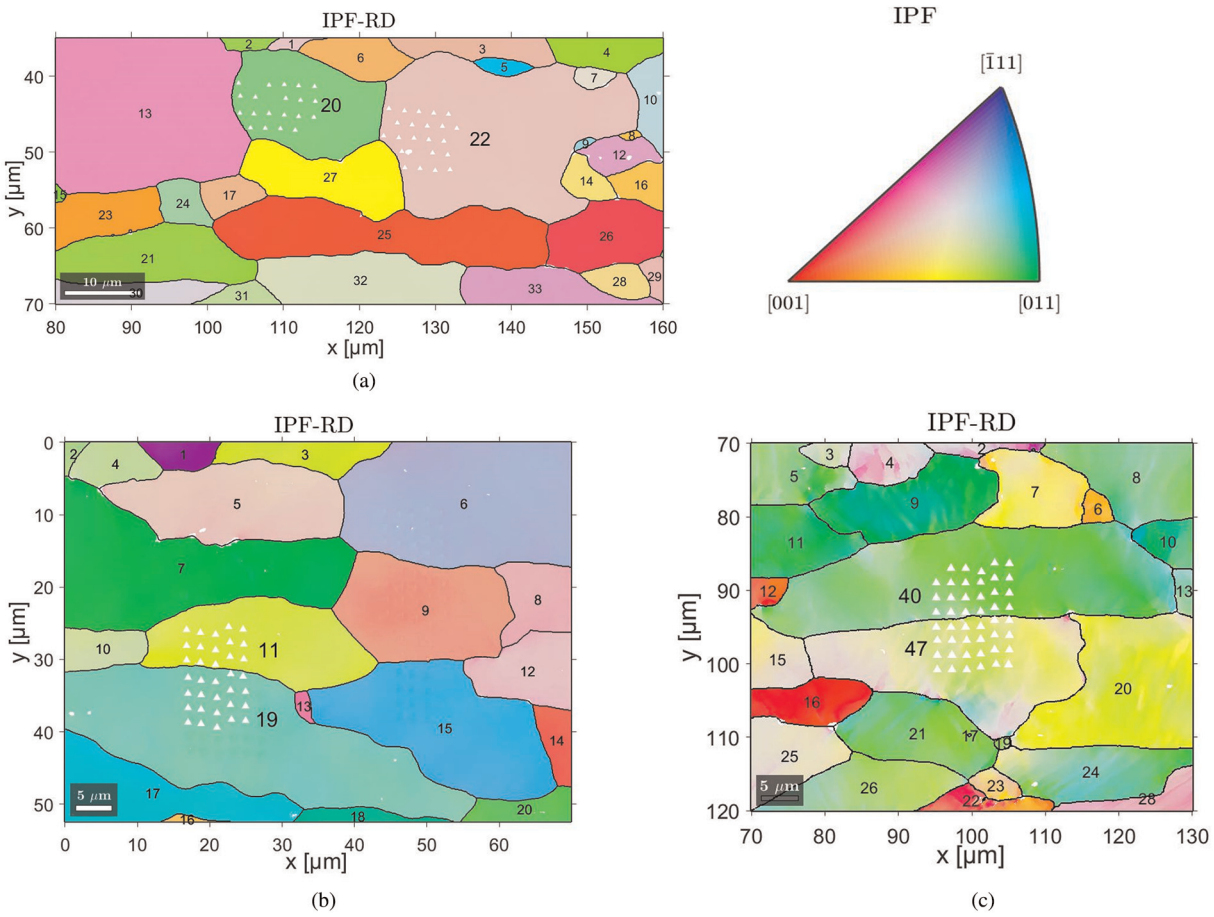

Fig. 2. Inverse pole figures along the RD direction of the undeformed specimen (a), the deformed specimen at 3% (b) and 18% (c) plastic strains, respectively. The indent locations are also reported at each plastic strain level.

where α_{OP} is a geometric constant, m is the power law exponent, and, h_p is the final depth after complete unloading. m is not a fixed value directly related to the tip geometry but varies in the range of 1.2 to 1.6 depending on the material [18,19]. For an accurate nanohardness calculation, the value of ε is obtained by the concept of "effective indenter shape" [19], which establishes a relationship between ε and m, where m is determined experimentally by a least squares fitting procedure. In our study, the exponent m was determined by a power law fit of the unloading curve between 98 and 40% of F_m and the corresponding values of ε vary between 0.74 and 0.79.

Nanoindentation tests were performed using the UltraNanoIndenter UNHT2 (Anton Paar). A well-calibrated Berkovich type tip was used for the tests. The tip calibration was performed on fused silica which is a standard isotropic material with well-known homogeneous Young's modulus ($E_{FS} = 73.2 \pm 0.3$ GPa) and Poisson ratio ($\nu_{FS} = 0.16$). The indentations were performed up to a maximum load of 1 mN corresponding to maximum depths ranging from 115 to 125 nm. The spacing between indentations was set between 2 and 2.2 µm to avoid the possibility of mutual interaction between the plastic zones of subsequent indentations [20]. The loading and unloading rates were set at 0.2 mN/s, with a holding time of 1 s at maximum load before unloading to minimize the effect of creep on the unloading curve. Indentations were performed along multiple parallel vertical lines roughly perpendicular to grain boundaries (see Fig. 2). However, the indents were not aligned horizontally so that nanohardness values at different distances separated by less than 2 µm from a given GB were obtained.

In this study, a mechanistic model similar to the one proposed by Durst et al. [21] is applied to estimate the total dislocation density from nanohardness values. For plastically flowing metals, the local measured nanohardness H can indeed be roughly estimated from the material's normal flow stress σ_f according to the Tabor's law [22]:

$$H \approx 3\sigma_f. \tag{7}$$

On the other hand, the resolved shear stress τ_f for plastic flow can be related to the initial resolved shear stress τ_0 and the total dislocation density ρ_T due to "forest"-type hardening using a Taylor's law [23]:

$$\tau_f = \tau_0 + \alpha_d \mu b \sqrt{\rho_T}, \tag{8}$$

where µ is the elastic shear modulus. Here, $\mu = 80$ GPa is used for a ferritic steel as in a previous study [1]. The constant α_d is an empirical factor depending on the dislocation arrangements. This factor is generally between

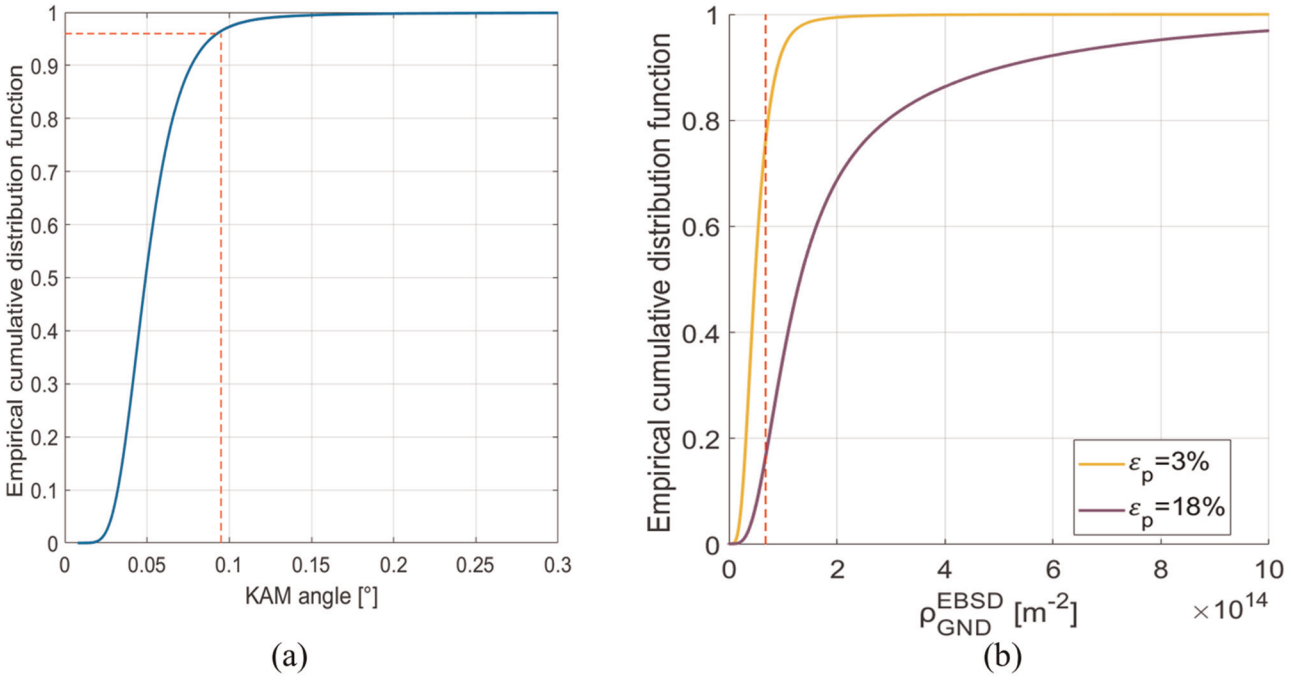

Fig. 3. Empirical cumulative distribution function of (a) KAM angle for undeformed Al-killed ferritic steel, (b) GND density determined by EBSD for 3% and 18% plastic strains, respectively.

0.2 and 0.4 [24]. In our case, the value $\alpha_d = 0.3$ is chosen. The total dislocation density is defined as $\rho_T = \rho_{GND} + \rho_{SSD}$, where ρ_{SSD} is the statistically stored dislocation density. Using a Taylor factor of M = 3 [21] to relate the crystal shear flow stress τ_f to the average normal flow stress σ_f, we have:

$$\sigma_f = \sigma_0 + M\alpha_d \mu b\sqrt{\rho_T}, \tag{9}$$

with $\sigma_0 \approx M\tau_0$ the initial tensile yield strength of the material computed at $\varepsilon_p = 0.2\%$ (identified as 175 MPa in Fig. 1). We have considered M as an average Taylor factor, which is assumed to be constant for each grain. Then, combining equation (7) together with equation (9) yields:

$$H \approx H_0 + 3M\alpha_d \mu b\sqrt{\rho_T}, \tag{10}$$

where H_0 is the macrohardness for the undeformed sample ($H_0 \approx 3\sigma_0$). Therefore, according to equation (10), the total dislocation density (expressed in m^{-2}) can be estimated from the value of nanohardness H as follows:

$$\rho_T \approx \left(\frac{H - H_0}{3M\alpha_d \mu b}\right)^2. \tag{11}$$

3 Results and discussion

3.1 EBSD Maps and GND densities

Inverse Pole Figure (IPF) maps obtained by EBSD in the rolling direction (RD) (also the tensile direction) are shown in Figure 2 along with the grain numbers and indentation positions at each considered tensile plastic strain.

First of all, it must be underlined that it is of great importance to evaluate the angular resolution of the EBSD data for an accurate determination of the GND density at low strains. This angular resolution can be determined from the local misorientation distribution or "Kernel Average Misorientation" (KAM) in an undeformed material [25]. Following [4], the angular resolution is defined by the 0.95 percentile of the cumulative KAM distribution function. Figure 3a represents the empirical cumulative distribution of the KAM angle, computed from the 8 nearest neighbors, and derived from the raw orientation data acquired on the Al-killed ferritic undeformed sample. Figure 3a shows that the 95th percentile of the KAM angle distribution is close to ∼0.1° as represented by the intersection of dotted red lines while the average KAM angle is 0.054°. The GND density defining the noise threshold "$\rho_{GND}^{noisethsd}$" for the undeformed Al-killed ferritic steel is then computed with an uncertainty of the orientation measurement $\Delta\theta \sim 0.1°$ and is given by [26]:

$$\rho_{GND}^{noisethsd} = \frac{\Delta\theta}{b\Delta x} \approx 7.0 \times 10^{13} m^{-2}, \tag{12}$$

where Δx is the step size of the EBSD map, which is here 100 nm. Figure 3b shows the evolution of GND density cumulated probability function with plastic strains. From this figure, the fractions of measured GND densities that are below the noise threshold, i.e., such that $\rho_{GND}^{EBSD} < \rho_{GND}^{noisethsd}$, are 80% for $\varepsilon_p = 3\%$ and reduce to 19% for $\varepsilon_p = 18\%$, as indicated by the dotted red line.

Figure 4 shows a map of GND densities obtained for $\varepsilon_p = 18\%$ and the locations of indents in a region crossing two grains with high GND densities at the grain boundary.

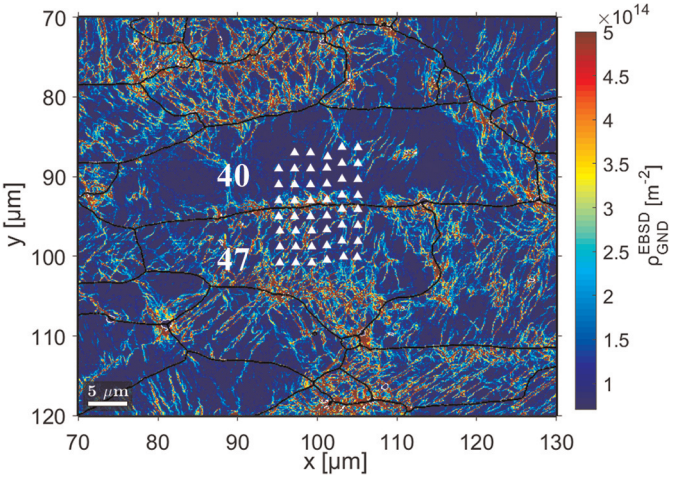

Fig. 4. GND density map of the Al-k specimen deformed at $\varepsilon_p = 18\%$. Indents in grains 40 and 47 are also reported (see Fig. 2c).

The concentration of GND densities is observed close to GB on both sides of grains 40 and 47 (see the grain numbers in Fig. 2c).

In order to investigate the effects of GB distance on nanohardness and GND densities, the minimum distance between each indentation mark center and EBSD pixel to the corresponding grain boundary was calculated with the MTEX software [14].

Figure 5 shows the variation of GND density, smoothed by a "moving average" computing with n = 15 points, along the different indentation lines that cross over the GB (see Fig. 4). The presence of a high density of GND near the GB and a decrease of this density as one moves away from the GB can be clearly noticed in grain 40 and 47. An increase of the GND density is observed far from the GB due to the presence of intra-granular dislocation cells formed at $\varepsilon_p = 18\%$.

3.2 Nanohardness measurements and total dislocation density profiles

Figure 6 represents nanohardness values measured by nanoindentation at different plastic strains with respect to the distance from the corresponding GB. The nanohardness measured at 0% does not vary much between the grain center and the GB. Therefore, the effect of GND densities induced by nanoindentation near GBs remains negligible.

An increase of nanohardness measurement is showed in the vicinity of the GB at 3% plastic strain compared to the undeformed case. A difference of nanohardness values between the region close to GB and the grain center can already be observed at 3%. This difference reaches a value of $\Delta H \approx 0.4$ GPa for grain 19 and $\Delta H \approx 0.3$ GPa for grain 11. This is in contrast with the values of GND densities deduced from EBSD, which are still almost all below the noise threshold at 3%, so that spatial gradients of GND densities cannot actually be analyzed at this strain level from EBSD data. However, the observed small gradient of nanohardness indicates that a GND density layer already

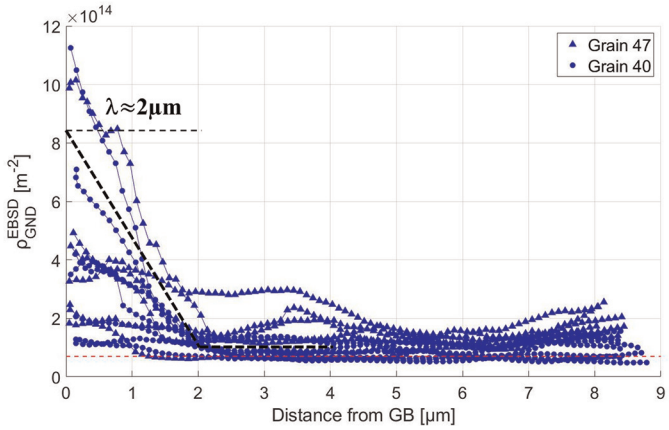

Fig. 5. Moving average with n = 15 of GND density measured by EBSD of specimens deformed at $\varepsilon_p = 18\%$ for grains 40 and 47. The red line represents the noise threshold of GND density, $\rho_{GND}^{noisethsd} = 7.0 \times 10^{13} m^{-2}$. The black dotted lines are a guide for the eye to estimate the thickness λ of the grain boundary affected layer.

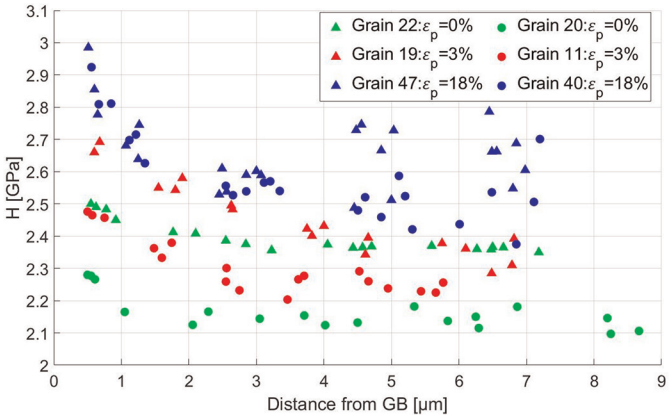

Fig. 6. Nanohardness H as a function of the distance from GB for the undeformed sample in grains 22 and 20; the deformed samples at $\varepsilon_p = 3\%$ in grains 11 and 19, and, at $\varepsilon_p = 18\%$ in grains 47 and 40.

starts to form at this small strain level through the increase of total dislocation density ρ_T (see Eq. (11)), which contains a larger part of ρ_{GND} in the GB-affected zone.

At $\varepsilon_p = 18\%$, close to the grain boundary 40-47, the nanohardness value is roughly identical on both sides of the boundary over a distance of about 2 μm. In such a region, the nanohardness is of the order of 2.8 GPa while beyond the nanohardness decreases to reach an average value of the order of 2.4 GPa in the center of the grain 40. In grain 47, an increase of hardness far from GB that correlates with the increase of GND density measured by EBSD is observed due to the presence of dislocation cells (see Fig. 4). A large difference of nanohardness values between the region close to GB over a distance of about 2 μm and the grain center is observed at 18%. This difference reaches a value of $\Delta H \approx 0.5$ GPa for grain 40 and $\Delta H \approx 0.6$ GPa for grain 47.

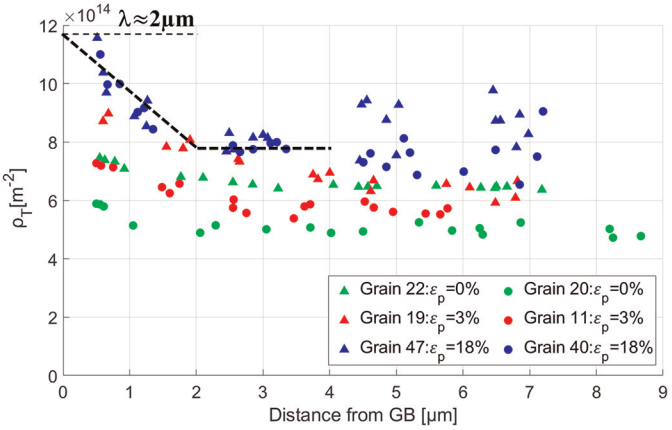

Fig. 7. Total dislocation density ρ_T estimated from H as a function of the distance from GB for the undeformed sample in grains 22 and 20; the deformed samples at $\varepsilon_p = 3\%$ in grains 11 and 19, and, at $\varepsilon_p = 18\%$ in grains 47 and 40. The black dotted lines are a guide for the eye to estimate the thickness λ of the grain boundary affected layer.

Table 2. Summarized comparisons about the capabilities of 2D-EBSD and Nanoindentation methods to detect spatial gradients of dislocation densities and estimate the internal length λ.

	GND from 2D-EBSD	Nanoindentation
Spatial resolution	0.1 μm	2 μm
Low plastic strain $<=3\%$	Not applicable	Gradients detected at $\varepsilon_p = 3\%$
Large plastic strain (18%)	Gradient of GND densities	Gradient of total dislocation densities
Induced internal length λ	≈ 2 μm	≈ 2μm

Figure 7 shows the total dislocation density ρ_T estimated from equation (11). In all grains, the values of ρ_T are larger than $5.10^{14}\,m^{-2}$. They are also larger that the GND density values obtained by EBSD (ρ_{GND}^{EBSD}), which demonstrates the consistency of the present mechanistic model. However, the total dislocation and GND densities display close values near grain boundaries, which shows that the formation of the grain boundary affected zone (GBAZ) of thickness λ is mainly due to GNDs (see Fig. 7 together with Fig. 5). From equation (11), ρ_T scales roughly as H^2 and thus exhibits similar qualitative trends as for the nanohardness values (Fig. 6).

Table 2 compares the two experimental methods in terms of capabilities regarding: spatial resolution, spatial gradients of dislocation densities (ρ_{GND}, ρ_T), and estimate of GND layer thickness λ in the vicinity of grain boundaries. From these summarized comparisons, it is seen that the spatial resolution is much higher for EBSD than for instrumented nanoindentation. Therefore, there is more statistical data provided by EBSD. However, the results show that the 2D EBSD method is limited at low strain levels (0 and 3%), while a gradient of the total dislocation density was observed at $\varepsilon_p = 3\%$ with the instrumented nanoindentation method. At high plastic strain, spatial GND and total density gradients were observed and correlated from both 2D-EBSD and nanoindentation methods. For both techniques and the grains studied, a layer of the order of 2 μm was found at sufficiently large plastic strains (here $\varepsilon_p = 18\%$, see Figs. 5 and 7).

4 Conclusions and perspectives

In this study, the accumulation of dislocation densities at grain boundaries in an Al-killed ferritic steel deformed at different plastic strains under uniaxial tension was experimentally investigated. The analyses of the GND density maps by 2D-EBSD and the total dislocation density profiles from nanohardness measurements lead to the following conclusions:

- The angular resolution of the EBSD data was estimated to be about 0.1°. This value was achieved by using high-resolution EBSD maps analyzed in refined accuracy mode and optimized surface preparation. At 3% of plastic strain, a limitation of the EBSD-2D method for determining the GND density was found since most of the values were below the noise level.
- During plastic deformation, the GND density increased and reached larger values close to the grain boundaries, as clearly observed in the case of Al-killed ferritic steel at $\varepsilon_p = 18\%$. A spatial correlation between the nanohardness measurements and the GND density determined by EBSD-2D was demonstrated.
- The measured nanohardness values increased during plastic deformation especially in the vicinity of grain boundaries. A spatial gradient of the nanohardness values between the grain boundary and the grain center was already detected at $\varepsilon_p = 3\%$ and was estimated to spread over an internal length λ of about 2 μm at 18% in the investigated grains.

– A clear spatial correlation was also found between the total dislocation density calculated from the nanohardness data and the GND density estimated from EBSD data. Therefore, the increase of the total dislocation density magnitude with plastic strain in the grain boundary affected zone (GBAZ) defined by the internal length λ is mainly due to the increase of GND density in the GBAZ.
– These obtained dislocation density estimates and value of λ can be used to improve the Internal Length Mean Field (ILMF) micromechanical models to capture grain size effects on the flow stress of ferritic steels [1].

References

1. J.M. Pipard, N. Nicaise, S. Berbenni, et al., A new mean field micromechanical approach to capture grain size effects, Comput. Mater. Sci. **45**, 604–610 (2009)
2. J.W. Signorelli, A. Roatta, N.S. De Vincentis, et al., Electron backscatter diffraction study of orientation gradients at the grain boundaries of a polycrystalline steel sheet deformed along different loading paths, J. Appl. Crystallogr. **50**, 1179–1191 (2017)
3. N.S. De Vincentis, A. Roatta, R.E. Bolmaro, et al., EBSD analysis of orientation gradients developed near grain boundaries, J. Mater. Res. **22**, (2019)
4. J. Genée, N. Gey, F. Bonnet, et al., Experimental and numerical investigation of key microstructural features influencing the localization of plastic deformation in Fe-TiB2 metal matrix composite, Mater. Sci. **56**, 11278–11297 (2021)
5. M. Calcagnotto, D. Ponge, E. Demir, et al., Orientation gradients and geometrically necessary dislocations in ultrafine grained dual-phase steels studied by 2D and 3D EBSD, Mater. Sci. Eng. A **527**, 2738–2746 (2010)
6. S.K. Mishra, P. Pant, K. Narasimhan, et al., On the widths of orientation gradient zones adjacent to grain boundaries, Scr. Mater. **61**, 273–276 (2009)
7. G.Z. Voyiadjis, M. Yaghoobi, Review of nanoindentation size effect: Experiments and atomistic simulation, Crystals **7**, 321 (2017)
8. W.D. Nix, H. Gao, Indentation size effects in crystalline materials: a law for strain gradient plasticity, J. Mech. Phys. **46**, 411–425 (1998)
9. G.Z. Voyiadjis, C. Zhang, The mechanical behavior during nanoindentation near the grain boundary in a bicrystal FCC metal, Mater. Sci. Eng. A **621**, 218–228 (2015)
10. C. Zhang, G.Z. Voyiadjis, Rate-dependent size effects and material length scales in nanoindentation near the grain boundary for a bicrystal FCC metal, Mater. Sci. Eng. A **659**, 55–62 (2016)
11. Y.M. Soifer, A. Verdyan, M. Kazakevich, et al., Nanohardness of copper in the vicinity of grain boundaries, Scr. Mater. **47**, 799–804 (2002)
12. W.A. Soer, Interactions between dislocations and grain boundaries, PhD Thesis, University of Groningen, 2006
13. J.S. Weaver, D.R. Jones, N. Li, et al., Quantifying heterogeneous deformation in grain boundary regions on shock loaded tantalum using spherical and sharp tip nanoindentation, Mater. Sci. Eng. A **737**, 373 (2018)
14. F. Bachmann, R. Hielscher, H. Schaeben, Grain detection from 2d and 3d EBSD data – Specification of the MTEX algorithm, Ultramicroscopy **111**, 1720–1733 (2011)
15. J.F. Nye, Some geometrical relations in dislocated crystals, Acta Metall. **1**, 153–162 (1953)
16. W. Pantleon, Resolving the geometrically necessary dislocation content by conventional electron backscattering diffraction, Scr. Mater. **58**, 994–997 (2008)
17. W.C. Oliver, G.M. Pharr, An improved technique for determining hardness and elastic modulus using load and displacement sensing indentation experiments, J. Mater. Res. **7**, 1564–1583 (1992)
18. W.C. Oliver, G.M. Pharr, Measurement of hardness and elastic modulus by instrumented indentation: Advances in understanding and refinements to methodology, J. Mater. Res. **19**, 3–20 (2004)
19. G.M. Pharr, A. Bolshakov, Understanding nanoindentation unloading curves, J. Mater. Res. **17**, 2660–2671 (2002)
20. P. Sudharshan Phani, W.C. Oliver, A critical assessment of the effect of indentation spacing on the measurement of hardness and modulus using instrumented indentation testing, Materials & Design **164**, 107563 (2019)
21. K. Durst, B. Backes, O. Franke, et al., Indentation size effect in metallic materials: Modeling strength from pop-in to macroscopic hardness using geometrically necessary dislocations, Acta Mater. **54**, 2547–2555 (2006)
22. D. Tabor, The hardness of solids, Rev. Phys. Tech. **1**, 145 (1970)
23. G.I. Taylor, The mechanism of plastic deformation of crystals. Part I: Theor. Proc. Roy. Soc. A **145**, 362 (1934)
24. H. Mughrabi, The α-factor in the Taylor flow-stress law in monotonic, cyclic and quasi-stationary deformations: Dependence on slip mode, dislocation arrangement and density, Curr. Opin. Solid State Mater. Sci. **20**, 411–420 (2016)
25. T. Friedrich, A. Bochmann, J. Dinger, et al., Application of the pattern matching approach for EBSD calibration and orientation mapping, utilising dynamical EBSP simulations, Ultramicroscopy **184**, 44–51 (2018)
26. A.J. Wilkinson, D. Randman, Determination of elastic strain fields and geometrically necessary dislocation distributions near nanoindents using electron back scatter diffraction, Philos. Mag. **90**, 1159–1177 (2010)

Cite this article as: Layal Chamma, Jean-Marc Pipard, Artem Arlazarov, Thiebaud Richeton, Jean-Sébastien Lecomte, Stéphane Berbenni, A combined EBSD/nanoindentation study of dislocation density gradients near grain boundaries in a ferritic steel, Matériaux & Techniques **110**, 203 (2022)